CrossMark

ORIGINAL RESEARCH

Influence of plastic deformation in flexible pad laser shock forming – experimental and numerical analysis

Balasubramanian Nagarajan[1,2] · Sylvie Castagne[1,2] · Zhongke Wang[1,3] · H.Y. Zheng[1,3] · Kartikeyan Nadarajan[2]

Abstract Flexible Pad Laser Shock Forming (FPLSF) is a new microforming process using laser-induced shock pressure and a hyperelastic flexible pad to induce high strain-rate ($\sim 10^5$ s^{-1}) plastic deformation on metallic foils to produce 3D microcraters. This paper studies the effect of two significant process parameters of FPLSF, flexible pad material and its thickness, on the deformation characteristics of the metal foils using experiments and finite element analysis. A finite element model is developed to simulate the FPLSF process. The stress-strain distribution across the foil and the flexible pad at different process stages of FPLSF are studied using FE analysis. Flexible pad materials including silicone rubber, polyurethane rubber, and natural rubber with thicknesses ranging between 300 μm and 3000 μm have been investigated in detail. Experimental results highlight that both the hardness and thickness of the flexible pad significantly influence the deformed crater geometry, thickness distribution across the formed crater and surface hardness at the crater surfaces. The experimental results are correlated with the stress-strain distributions from finite element analysis to study the underlying behaviors.
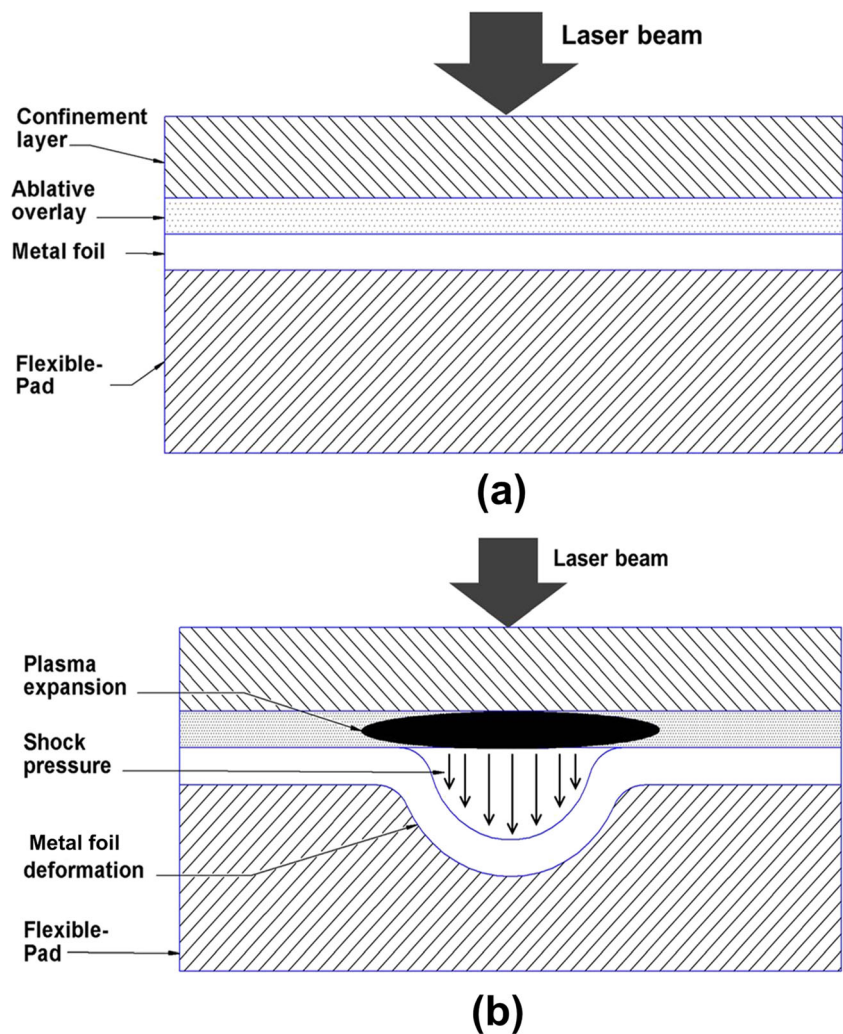
✉ Sylvie Castagne
scastagne@ntu.edu.sg

1 SIMTech-NTU Joint Laboratory (Precision Machining), Nanyang Technological University, 50 Nanyang Avenue, Singapore 639798, Singapore

2 School of Mechanical and Aerospace Engineering, Nanyang Technological University, 50 Nanyang Avenue, Singapore 639798, Singapore

3 Machining Technology Group, Singapore Institute of Manufacturing Technology, 71 Nanyang Drive, Singapore 638075, Singapore

Introduction

The demand for new microfabrication techniques is ever-increasing with evolving requirements for customization of materials and feature shapes. Recently, Flexible Pad Laser Shock Forming (FPLSF) has been developed to fabricate 3D microscale features on thin metal foils [1]. This technique is applicable for the production of microcomponents in various fields including optics, electronics, and biomedical devices. Fig. 1a illustrates the schematic of FPLSF. Plastic deformation of metallic foils in FPLSF is achieved using laser-induced shock waves and a flexible pad. The metal foil to be deformed is covered with ablative overlay, a sacrificial coating layer. Upon laser irradiation, the ablative overlay is vaporized instantaneously and generates high density and high pressure plasma. The expansion of the plasma in the direction opposite to the metal foil is restricted by the confinement layer, a transparent material on top of the ablative overlay. The plasma expansion induces shockwaves towards the metal foil. The metal foil experiences plastic deformation when the laser-induced shock pressure exceeds the dynamic yield strength of the foil material. The metal foil is placed over the flexible pad, a hyperelastic material, which undergoes large elastic deformation along with plastic deformation of the metal foil. Hemispherical deformation craters are formed on the metal foil using FPLSF as shown in Fig. 1b.

FPLSF involves several process variables including laser fluence, pulse duration, number of laser pulses, pulse width, and beam profile, which correspond to the laser characteristics. In addition, the material properties and thicknesses of the metal foil, ablative overlay, confinement layer and flexible

Fig. 1 Schematic of **a** flexible pad laser shock forming (FPLSF) setup, **b** plastic deformation of metal foils in FPLSF

pad could play a significant role. The effects of some process parameters such as laser fluence, number of pulses, confinement layer material, and confinement thickness on the deformation features have been investigated experimentally [2]. In FPLSF, the flexible-pad supports the metal foil and undergoes hyperelastic deformation during shock loading. Therefore, in order to understand the FPLSF process characteristics, the influence of the flexible pad on the plastic deformation of the metal foil needs to be investigated extensively.

FPLSF can be comparable to Rubber Pad Forming (RPF), which uses rubber dies and metal punches for sheet metal deformation, instead of flexible pad and non-contact laser-induced shockloading in FPLSF. Typical materials used as the rubber pad in RPF include natural rubber, silicone rubber, and polyurethane rubber [3–5]. Ramezani et al. [3] compared various materials as flexible punches in sheet metal forming and identified silicone rubber as an appropriate material for a small number of loading cycles which required lower punch load, whereas polyurethane rubber was found to be suitable for a large number of loading cycles. Liu et al. [6] observed no

change in von Mises stress distribution on the blank and the die filling ratio with a change in rubber pad shore hardness, highlighting insignificant effect of pad hardness on material formability. Peng et al. [7] observed similar stress profile and thickness distribution of the formed blank with a change in the rubber hardness during flexible punching process. A similar behavior was also identified with flexible forming of stainless steel sheets using polyurethane rubber pads [8]. In contrary to the above-mentioned findings of an insignificant influence of the rubber hardness on deformation process, the maximum von Mises stress of the blank was found to increase along with the increase in rubber hardness [9]. In laser dynamic flexible forming, the filling capacity of the rubber increased with a reduction in hardness [10]. Lim et al. [11] also observed an increase in the forming depth with a reduction in the rubber hardness, as a corresponding increase in counter pressure facilitated the metal flow into the die. In sheet metal punching using urethane elastomers, an optimum pad hardness was prescribed, as insufficient punching occurred with the hardness either too small or too high [12]. From the previous research

works, the rubber hardness is found to have significant influence on the stress-strain distribution of the metal blanks and the deformed feature geometry.

Though the effect of rubber pad hardness on the deformation depth in RPF processes has been studied extensively, there are limited studies on its influence on the thickness distribution of the formed features. Son et al. [13] observed a reduction in thinning of Al1050 sheets with an increase in rubber hardness during RPF. Contrarily, more thinning of aluminum sheets occurred with increase in the rubber hardness [3]. Despite the contradicting results, it is evident that the hardness of the rubber pad affects the thickness distribution of formed features.

The thickness of the rubber pad is also considered to be a significant process parameter in rubber pad forming processes [11, 12, 14]. The minimum thickness of the rubber pad is prescribed to be 2 or 3 times greater than the deformation depth in RPF [5, 15]. The increase in rubber pad thickness resulted in the reduction of deformation depth of metal sheets in laser dynamic flexible forming [10]. Lim et al. [11] observed a saturation of deformation depth when the pad thickness attained a threshold limit, highlighting the existence of an optimum pad thickness to maximize the deformation.

Despite the availability of literature on rubber pad from rubber pad forming, application of results for FPLSF could be critical due to the differences in process configuration between FPLSF and RPF. FPLSF uses non-contact laser shock loading, whereas RPF uses rigid metallic punches/dies. Furthermore, FPLSF has different deformation mechanisms due to high strain rate loading conditions, compared to quasi-static loading in rubber pad forming. Another significant difference between FPLSF and RPF is the deformation scale of the formed features, as FPLSF produces microscale deformation features, whereas macroscale deformation is realized with RPF. The influence of size effects is expected to play a significant role in the deformation behaviors. Therefore, the effect of hardness and thickness of the flexible pad on plastic deformation characteristics of the metal foil during FPLSF needs to be investigated. In addition, influence of the rubber pads on surface hardness, a significant mechanical property of the deformation features, has been rarely reported for rubber pad forming or similar processes.

In FPLSF, deformation of the metal foil occurs at strain rates greater than 1×10^5 s^{-1}. At these process speeds, it is difficult to study the process evolution and stress-strain distributions during the deformation experimentally. Furthermore, it will be time-consuming and difficult to extensively investigate a wide range of various process variables experimentally, to understand their influence on the metal foil deformation. Therefore, process simulation of FPLSF is necessary to predict the process outputs, analyse the process variables, and

study the characteristics of high strain rate deformation of the metal foil and the flexible pad.

This paper reports on the experimental investigation and numerical simulation of flexible pad laser shock forming. A Finite Element (FE) model is developed first to simulate the FPLSF process. The FE model is then validated by comparing the predicted shape and dimensions of the features with those of experiments at different laser fluences. A time-resolved analysis of stress-strain distribution at different foil positions is performed to understand the different process stages in FPLSF. Then, the effects of flexible pad materials on the crater profile, foil thinning at crater center, and hardness at the top and bottom crater surfaces are experimentally investigated for three different flexible pad materials, silicone rubber, natural rubber and polyurethane rubber. The experimental analysis of deformation behavior with change in the flexible pad thickness is discussed subsequently. The experimental results of flexible pad influence on the foil deformation are analyzed in detail using numerical simulation.

Experimental setup

A Q-switched, high power, Nd:YAG pulsed-laser with the following specifications was used for the laser irradiation: wavelength = 1064 nm, pulse duration =38 ns, maximum laser pulse energy =75 mJ at 6 KHz frequency. The laser beam was square-shaped (600 μm × 600 μm) with a flat-top intensity profile. In this study, the following three different materials with 25 μm thickness were used as the substrate: 99.9 % pure copper, 99.9 % pure nickel, and AISI316 stainless steel. The ablative overlay is made of a 15 μm thickness aluminum foil, which is placed over the metal foil. Deionized water with 4 mm thickness was used as the confinement layer. A thin layer of vacuum grease was applied between the metal foil and ablative overlay to provide perfect sealing. Silicone rubber, natural rubber, and polyurethane rubber were used as the flexible pad in this analysis.

Crater dimensions were measured using a Talyscan 3D surface profiler through scanning the top crater surface with a stylus probe (2 μm radius diamond tip). Scanning Electron Microscope (SEM) was used to visualize the crater surfaces.

The thickness distribution of deformed foils was characterized by sample thinning percentage using Eq. (1).

$$\text{Thinning } (\%) = \frac{t_0 - t_i}{t_0} * 100 \qquad (1)$$

where t_0 is the initial foil thickness and t_i is the foil thickness after FPLSF. The thickness at the crater center was measured by cross-sectioning the sample at 2 mm offset in the center, cold-mounting, grinding and polishing up to the crater center.

An optical microscope was used to measure the foil thickness. The initial foil thickness (t_0) was 31.8 μm with a standard deviation of 1.28 μm. Thinning measurement at the crater center (position 3 in Fig. 2a) is used in this analysis.

Vickers Microindenter was used to measure the hardness of the sample surfaces. The indentation (50 Kgf load) was applied at the center of the crater at both the top and bottom surfaces as illustrated in Fig. 2b. While measuring the bottom crater surface, the crater was filled with resin hardener in order to ensure that the crater do not experience bending during indentation. Both the top and bottom surfaces of the foil were polished before FPLSF to eliminate the effect of surface roughness on the indentation. The percentage change in hardness is used in the analysis for better comparison. The experiments were repeated three times and the average values are presented.

Numerical simulation

Process modeling

FPLSF involves three significant physical behaviors which require modelling: laser-induced shockwave formation, plastic deformation of metal foils, and hyperelastic deformation of flexible pad.

Laser-induced shock pressure

Fabbro et al. [16] modelled the pressure of shockwaves induced by the expanding plasma under confining conditions. Fabbro shock pressure model has been extensively used in laser-induced shock pressure simulations [10, 17, 18]. This model is based on the assumption that two shockwaves propagate inside the target and the confinement, with fluid velocities behind the shockwave as $u_1(t)$ and $u_2(t)$ respectively. The plasma thickness at the interface between target and confinement, [$L(t)$] is a function of time and fluid velocities which

is given by, $L(t) = \int_0^t [u_1(t) + u_2(t)] \, dt$. Using the shockwave relation for pressure, $P = u_i Z_i$ with $i = 1$ or 2, the derivative of $L(t)$ can be obtained as,

$$\frac{dL(t)}{dt} = \frac{2}{Z} P(t) \tag{2}$$

where $2/Z = 1/Z_1 + 1/Z_2$; Z_1 and Z_2 are shock impedances of the target and the confinement materials, respectively. The incident laser energy (I) on the target is converted into work to increase the plasma interface and its internal energy which is formulated in Eq. (3).

$$I(t) = \frac{dL(t)}{dt} P(t) + \frac{3}{2\alpha} \frac{d}{dt} [P(t)L(t)] \tag{3}$$

in which α is the fraction of the internal energy in the form of thermal energy. Considering constant laser intensity (I_0), the peak shock pressure (GPa) can be calculated using Eq. (4).

$$P = 0.01 \left(\frac{\alpha}{3 + 2\alpha} \right)^{0.5} \sqrt{I_0 \, Z} \tag{4}$$

The laser-induced shock pressure as a function of time was calculated by numerically solving the Eqs. (2) and (3) using MAPLE code. In this analysis, the calculated shock pressure was applied directly on the top surface of the metal foil. The spatial distribution of shock loading was assumed to be constant as the flat-top beam profile was used in the experiments. The following material parameters were used to calculate the shock pressure: $\alpha = 0.1$, Z_1 (Aluminum) $= 1.5 \times 10^6$ g cm^{-2} s^{-1} and Z_2 (Water) $= 0.165 \times 10^6$ g cm^{-2} s^{-1} [19].

Plastic deformation of metal foils

As laser shock forming processes typically involve ultra-high strain rate plastic deformation, the corresponding constitutive models should include the strain rate effects. Johnson-Cook constitutive model is developed for materials subjected to high temperature, large strains, and high strain rates [20]. This

Fig. 2 **a** Thickness measurement positions along the crater cross-section, **b** schematic of surface hardness measurement method

(a)

(b)
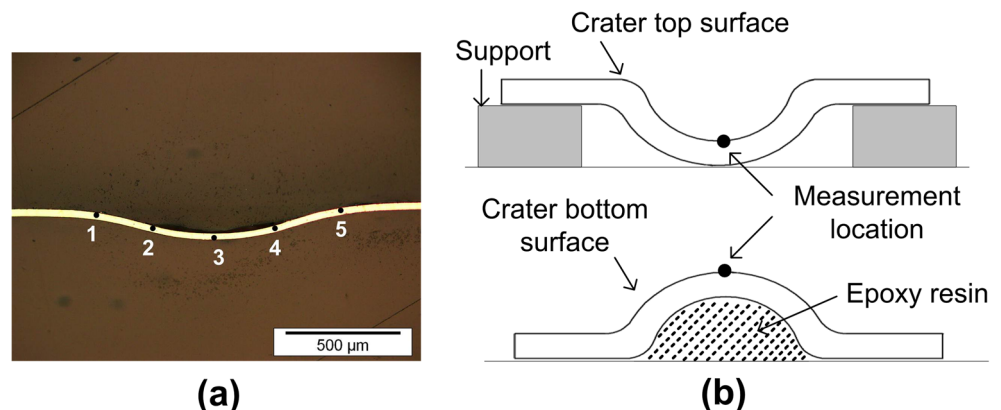
model has been extensively used to model materials that experience strain rates up to $10^5 \, s^{-1}$ during deformation. The von Mises flow stress (σ) is calculated from Eq. (5).

$$\sigma = \left[(A + B\varepsilon^n) \left(1 + C ln\left(\frac{\dot{\varepsilon}}{\dot{\varepsilon}_0} \right) \right) \right] \left[1 - T^{*m} \right] \qquad (5)$$

where homologous temperature T^* is given by $T^* = \frac{T - T_r}{T_m - T_r}$, in which T_r and T_m are reference and melting temperatures respectively. A, B, C, m and n are material constants, in which A is the yield stress, B and n represent the work hardening effect, C denotes the strain-rate effect, and m includes the temperature effect on the flow stress. ε, ε, and ε_0 are strain, strain rate and the reference strain rate respectively. The temperature effects are not considered in this analysis. The material properties and Johnson-Cook parameters of the metal foils are given in Table 1.

Hyperelastic deformation of flexible pad

The flexible pad used in FPLSF possesses hyperelastic material properties, which undergo large elastic deformation upon loading. To define the hyperelastic material properties of the rubber, different models including Yeo, Mooney-Rivlin, Ogden, Neo-Hookien, Humphrey, and Martins have been developed [23]. Mooney-Rivlin model has been widely used in several studies to define the deformation of rubbers [6, 9, 10, 14, 23]. The hyperelastic models are based on strain energy formulation, in which stress component (σ_{ij}) is defined as the derivative of strain energy function (W) with respect to the strain component (ε_{ij}),

$$\sigma_{ij} = \frac{\partial W}{\partial \varepsilon_{ij}} \qquad (6)$$

$$W = \sum_{k+m=1}^{n} C_{km} \left[(I_1 - 3)^k + (I_2 - 3)^m \right] + \frac{1}{2} K(I_3 - 1)^2 \qquad (7)$$

where C_{km} represents the material constants, I_1, I_2, and I_3 are the strain component invariants, and K is the bulk modulus. In this analysis, stress - strain data of the flexible pad materials from uniaxial compression test (loading rate = 0.5 mm/min, limiting strain =0.8) was supplied as the input for the Mooney-Rivlin strain energy formulation. The compression test

specimens were prepared according to ASTM D395 standard. The stress-strain curves for silicone rubber, natural rubber, and polyurethane rubber from uniaxial compression test are shown in Fig.3. The hardness (Shore A) values of polyurethane rubber, silicone rubber and natural rubber are 70, 60, and 42, respectively.
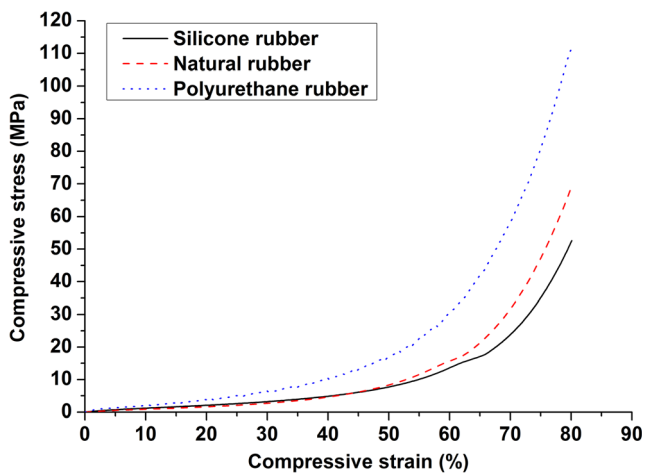
Simulation setup

Abaqus/Explicit finite element code is used in this study to perform the FPLSF simulation. As the shock loading profile is assumed to be identical to that of the laser beam profile, the square laser beam requires 3D modelling of the process. However, a quarter of the 3D model is sufficient and used for the simulation to reduce the computational cost.

The 3D finite element model of FPLSF consisting of metal foil, flexible pad, and metal support, is shown in Fig. 4a while Fig. 4b shows the foil positions at the center and the circumference of the crater, where stress and strain distributions are analyzed. The flexible pad was placed over the rigid metal support. Both the foil and the flexible pad were modelled as deformable solids, where the part dimensions were given according to the experimental setup. The metal foil and the flexible pad were defined using C3D8R element, which is an 8-node, linear brick element with reduced integration and hourglass control. The mesh sizes for the foil and the flexible pad are 5 and 30 μm, respectively in all directions.

The interactions between the flexible pad and the metal foil, and between the flexible pad and the metal support, were defined using surface to surface contact algorithm. Friction coefficient of 0.4 was applied to define the friction between two contact surfaces: flexible pad and metal foil, flexible pad and metal support. Symmetric boundary conditions were applied on x-0-z and y-0-z surfaces for both the foil and the flexible pad. Temporal distribution of shock pressure calculated from the Fabbro model for various laser intensities is shown in Fig. 4c. Shock loading was applied on top of the copper foil (area over 0.3 mm × 0.3 mm) with uniform spatial distribution. The shock pressure duration used in this analysis was 200 ns as the shock pressure is found to last for 3 to 5 times the laser pulse width approximately [24]. The computation time of the entire simulation was set as 25 μs.

Table 1 Mechanical properties of foil materials

| Material	Density (Kg/m³)	Young's modulus (GPa)	Poisson's ratio	A (MPa)	B (MPa)	n	C
Cu [20]	8920	126	0.34	90	292	0.31	0.025
Ni [21]	8890	207	0.31	163	648	0.33	0.006
AISI316 [22]	7800	202	0.3	514	514	0.508	0.042

Fig. 3 Stress-strain curves for different flexible pad materials (Uniaxial compression)

Deformation analysis

Figure 5 compares the 3D and 2D geometries of the formed craters on the copper foil between experiment and simulation. SEM image of the formed crater, which is hemispherical in shape, for the laser fluence of 13.6 J/cm^2 with silicone rubber (900 μm thick) as the flexible pad is shown in Fig. 5a. It can be observed from the axial displacement contour of the metal foil (Fig. 5c) from simulations that the predicted crater shape is hemispherical, confirming the experimental observations. The formation of hemispherical crater profiles with the square-shaped laser beam is due to the spherical propagation of laser-induced plasma, as observed experimentally using a high speed camera [25]. The 2D (x-z plane) profile of the crater from simulation is compared with the surface profile measured by Talyscan surface profiler in Fig. 5b and d. From the simulations, the crater depth of 85.9 μm for the laser fluence of 13.6 J/cm^2 is predicted, whereas the corresponding crater depth from the experiments has been 97.8 μm. The difference in crater depth and crater diameter between simulation and experiment for 13.6 J/cm^2 fluence is found to be 12 and 4.8 % respectively. Fig. 5e compares the crater depth between experiment and simulation for laser fluence ranging between 7.3 and 20.9 J/cm^2. The discrepancy is attributed to a number of factors including limitations with shock pressure modeling, test data from quasi-static uniaxial deformation mode, and approximations in pressure pulse duration and loading area. The agreement between the experiments and simulation is reasonably sufficient for this study, as this papers focuses on examining the time-resolved stress-strain distributions during the process and analyzing the generic qualitative behavior of process parameters on the deformation characteristics using the process simulation. Thus, the developed finite element model is used for further analysis.

Firstly, evolution of the crater formation in FPLSF is analyzed in detail using finite element analysis. Fig. 6 shows the axial displacement profiles of copper foil and flexible pad (silicone rubber) at different time periods during the process. The corresponding laser fluence is 13.6 J/cm^2 and silicone rubber thickness is 900 μm. The crater formation in the metal foil can be classified into four stages as follows: (1) Metal foil deformation phase (up to 1.8 μs) (2) Flexible pad elastic deformation due to inertia (1.8 – 4.1 μs) (3) Flexible pad retraction (4.1 – 9 μs) (4) Foil detachment from the flexible pad (after 9 μs). The different process stages are also illustrated in
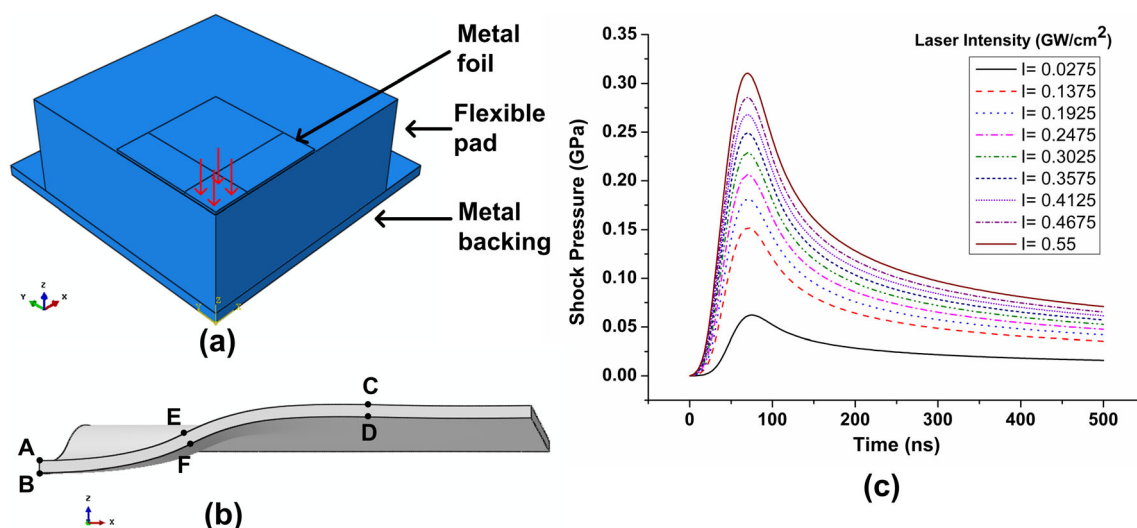
Fig. 4 **a** 3D finite element model of FPLSF process, **b** measurement set positions in metal foil for analysis, **c** temporal profile of laser-induced shock pressure calculated from Fabbro's Model [16] for different laser intensities

Fig. 5 Comparison of deformation feature on copper foil between simulation and experiment: **a** SEM image of the deformation crater top surface **b** 2D surface profile at the center of crater, from experiments; **c** 3D axial displacement (μm) contour **d** 2D (*x-z* plane) displacement (μm) profile of the foil, from simulations; at 13.6 J/cm^2 laser fluence, **e** comparison of crater depth between experiment and simulation for different laser fluence
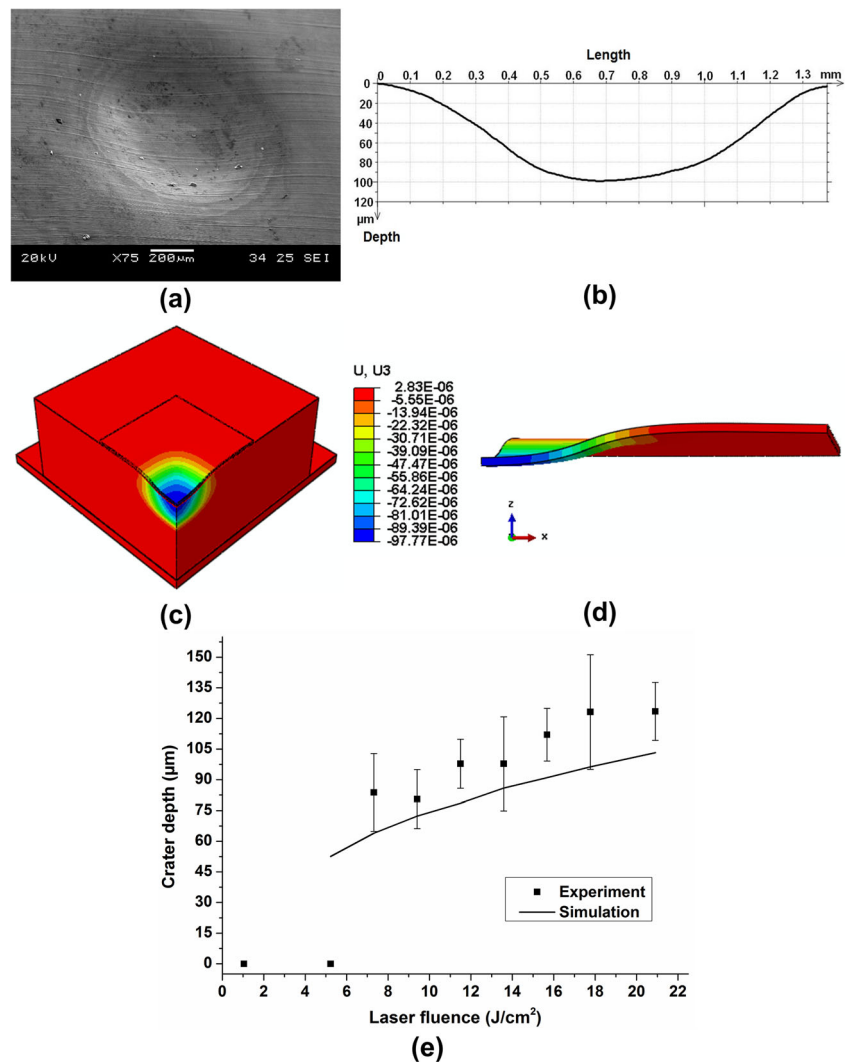

Fig. 7a, which compares the axial displacement of the foil and the flexible pad at center of their top surfaces.

Stage 1 (up to 1.8 μs): There is no significant deformation of the foil until 40 ns although the loading is started. The shockwaves start from the foil top surface, propagate through the foil thickness, and reflect back from its bottom surface, during which the next shockwave starts propagating from the top surface. The maximum von Mises stress occurs initially at the center of the foil thickness near the circumference of the loading area. This behavior can be observed in Fig. 7b through the early rise of equivalent plastic strains at foil positions E and F. After 110 ns, the location of maximum von Mises stress moves from the circumference to the regions adjacent to foil positions E and F. With increase in time, maximum von Mises stress location moves further away from the circumference to the foil center. Correspondingly, axial displacements at

positions A and B start respectively at 50 and 180 ns, and then increase gradually. Simultaneously, the shockwaves propagate in the transverse directions along the loading surface. It is interesting to observe that the foil deformation continues until 1.8 μs though the load duration ends at 200 ns. During this entire stage (until 1.8 μs), axial displacements of the foil and the flexible pad are similar, which can be verified from Figs. 6a and 7a.

Stage 2 (1.8 – 4.1 μs): The foil displacement saturates after 1.8 μs and increases slightly to reach its peak at 3.1 μs. Meanwhile, the flexible pad continues its displacement, as seen in Figs. 6b and 7a. The maximum von Mises stress at this stage is located near the crater edges in the foil, whereas it occurs at a distance of 300 μm from the flexible pad top surface. During this stage, elastic deformation of the flexible pad is continued till the shockwave reaches its bottom surface at 4.1 μs due to inertia.
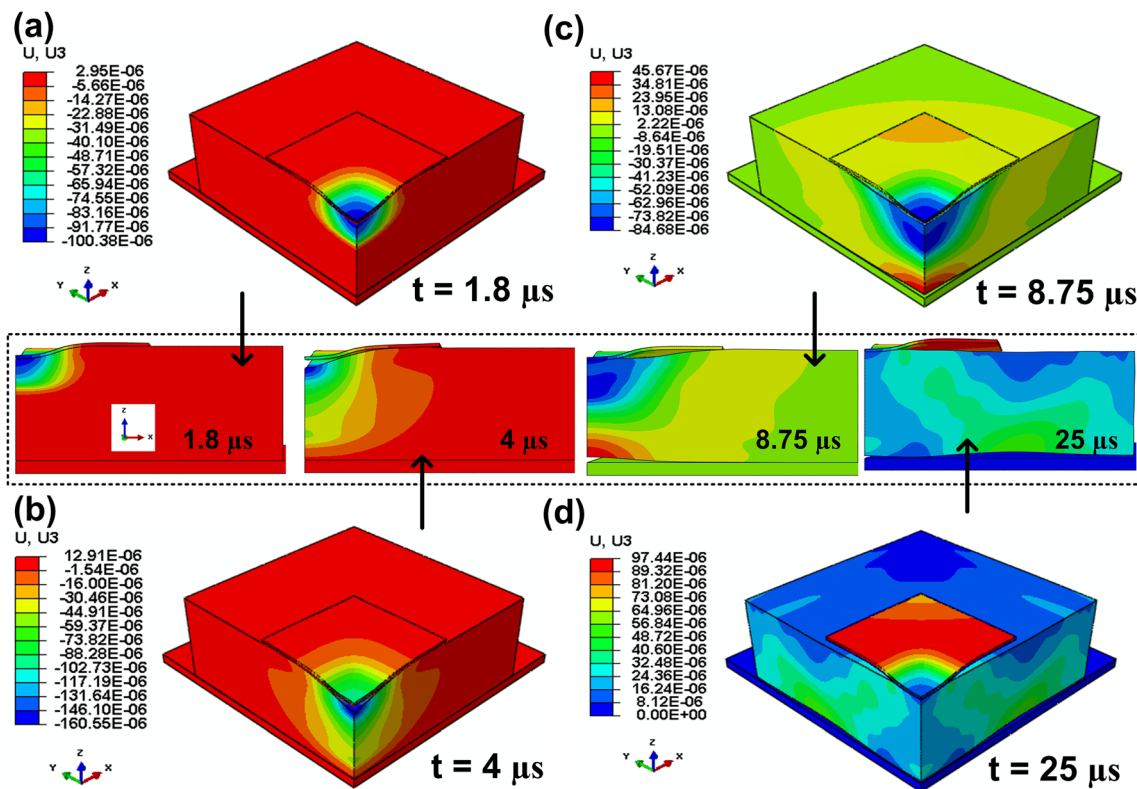
Fig. 6 Axial displacement (μm) contour with respect to time **a** t = 1.8 μs, **b** 4 μs, **c** 8.75 μs, **d** 25 μs; [Laser fluence – 13.6 J/cm²; Flexible pad - Silicone rubber (900 μm thick)]

Stage 3 (4.1 – 9 μs): The shockwaves retract back from the bottom surface after 4.1 μs, forcing the pad in the opposite direction. The pad comes into contact with the foil at 8.75 μs, as seen in Fig. 6c. Once the flexible pad contacts the foil at the center, both the foil and the pad are found to displace axially upwards. At this stage, a minor plastic deformation occurs only at the foil position B which could reduce the crater thickness. This behavior can be witnessed on Fig. 7b through the rapid increase in equivalent plastic

strain at position B after 8 μs. However, the shape of the crater still remains hemispherical as seen in Fig. 6c.

Stage 4 (after 9 μs): The axial displacement of the flexible pad and the foil continues upwards at this stage, as the foil is gradually detached from the flexible pad. However, the foil does not experience any plastic deformation. The formed crater on the metal foil, which is completely detached from the flexible pad at 25 μs, can be noticed in Fig. 6d.
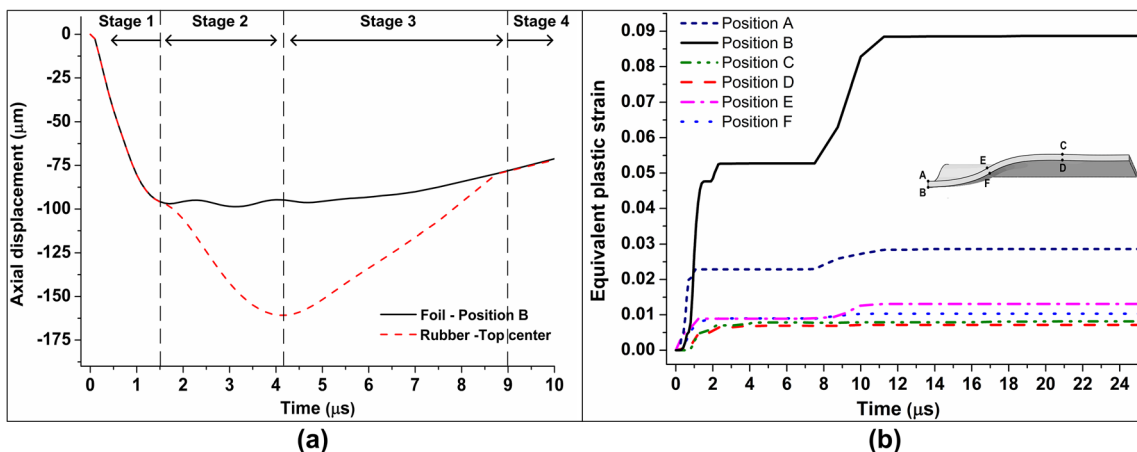
Fig. 7 **a** Comparison of axial displacement (μm) of the foil position B and center of the flexible pad top surface, **b** equivalent plastic strain with respect to time, for different foil positions

Results and discussions

Effect of flexible pad hardness

To study the effect of flexible pad material on the metal foil deformation, three different rubber materials, silicone rubber (SR), natural rubber (NR), and polyurethane rubber (PU) were tested. The thickness of the flexible pad was kept constant as 900 μm in this study. The experimental and finite element analyses are compared for different metal foils including copper, nickel and stainless steel.

Figure 8 shows the FPLSF experimental results of crater depth, thinning at the formed crater center, and top and bottom surface hardness at the crater center with change in flexible pad hardness. The three materials are sorted according to their shore hardness as follows: polyurethane rubber (70) > silicone rubber (60) > natural rubber (42).

The effect of flexible pad material on the crater depth for three different foil materials is shown in Fig. 8a. A reduction in crater depth with an increase in flexible pad hardness was observed irrespective of the foil material tested. It is obvious that the harder flexible pad has more restriction on the foil deformation.

Figure 9 compares the evolution of crater formation between flexible pad materials through axial displacement contour at different time periods during deformation. The simulation results are consistent with the experimental results, where the foil deformation reduces with the increase in the flexible pad hardness. It can be observed from Fig. 9 that the initiation and time duration of the four different stages of FPLSF process vary significantly with the flexible pad material. The flexible pad detaches from the foil at 1.4 μs with polyurethane rubber as compared to 1.8 μs for silicone rubber and natural rubber. This effect can be verified from Fig. 10a where axial displacements of the foil position B (center of the crater bottom surface) and center of the flexible pad top surface are compared between different flexible pad materials. The propagation of shockwave is observed to be faster with polyurethane rubber, which has the highest hardness. Correspondingly, elastic recovery of the pad too is faster with polyurethane rubber. This behavior can be witnessed from Fig. 10b where equivalent plastic strain at foil position B raises sharply at 7.5 μs for silicone rubber and natural rubber, whereas it increases at 5.6 μs for polyurethane rubber, the time at which the flexible pad comes in contact with the foil. Thus, the change in process stages for different flexible pads can be attributed to
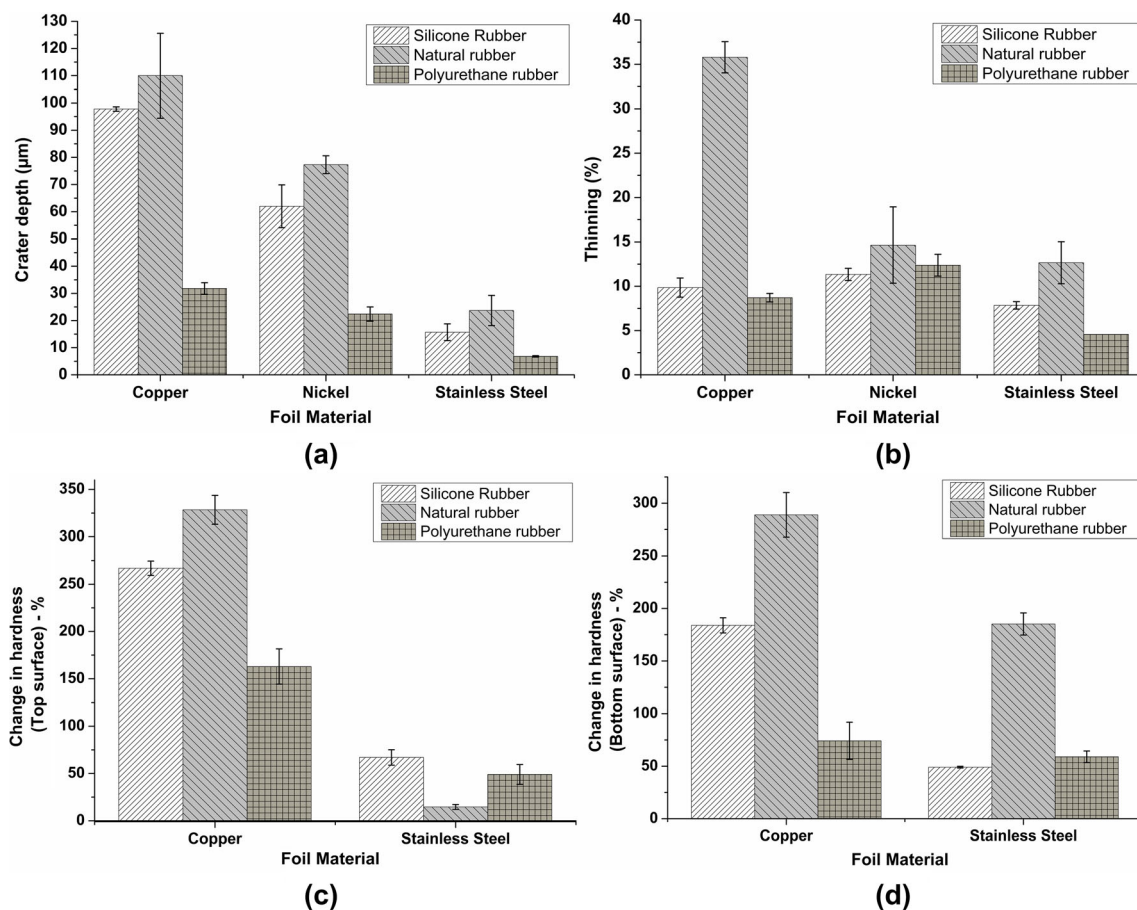
Fig. 8 Experimental investigation of the effect of flexible pad material on **a** crater depth, **b** foil thinning at crater center, **c** crater top surface hardness at the center, **d** crater bottom surface hardness at the center
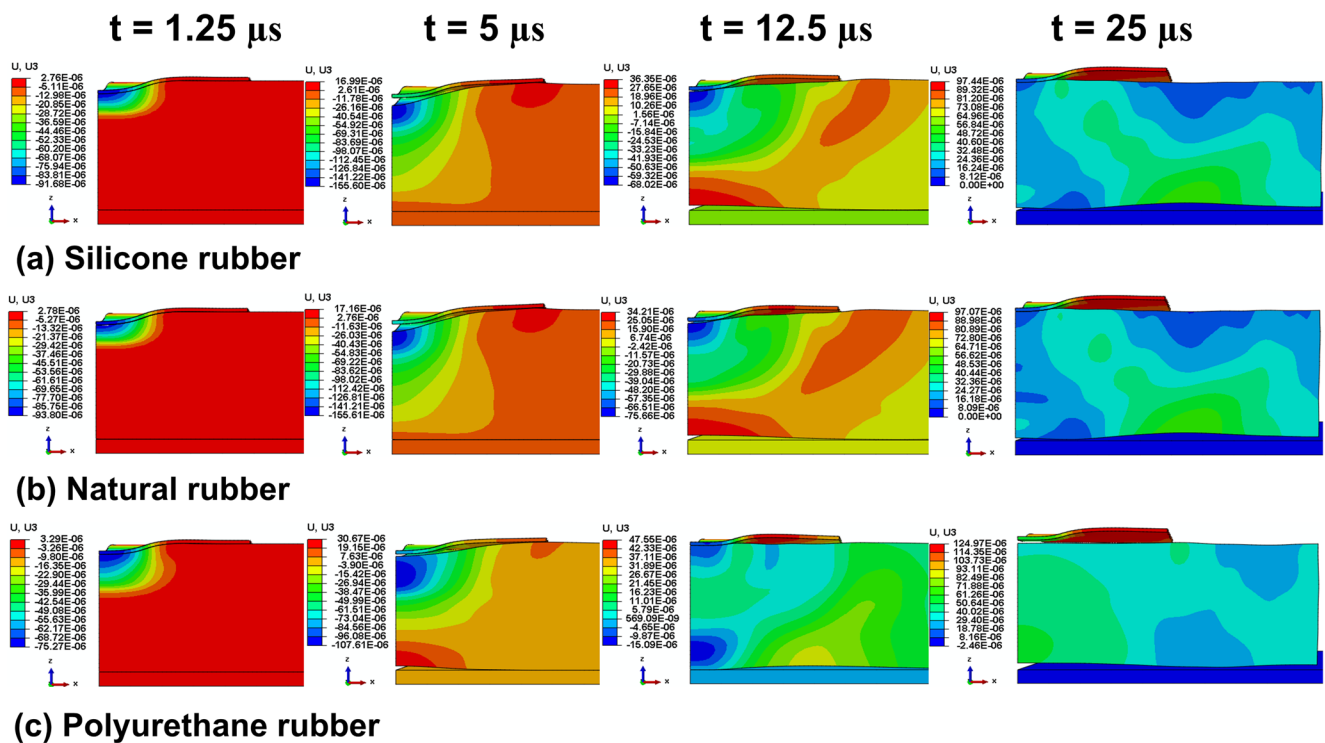
Fig. 9 Finite element analysis of the effect of flexible pad material on axial displacement (μm) contour at different time periods for **a** silicone rubber, **b** natural rubber, **c** polyurethane rubber

the corresponding change in propagation speed and direction of the shockwaves within the flexible pad.

As a result of plastic deformation of the metal foil in FPLSF, the foil experiences a reduction in thickness. The maximum thinning was found to occur at the crater center. Fig. 8b compares foil thinning at the center of the crater for different flexible pad materials. It is evident that foil thinning decreases with increase in flexible pad hardness for copper and stainless steel foils. Finite element simulation predicted the similar trend of thinning with the change in flexible pad material.

Figure 8c and d show the effect of flexible pad hardness on the crater hardness at the top and bottom surfaces. A reduction

in hardness at both the top and bottom crater surfaces was observed with increase in flexible pad for copper foil. Except a discrepancy with natural rubber pad, a similar trend can also be observed for the stainless steel foil. It is evident that the hardness at both the top and bottom foil surfaces increases as a result of FPLSF, irrespective of metal foil and flexible pad. The hardness at the top surface was found to be greater than that of bottom surface.

The experimental observation of reduction in foil thinning and the crater surface hardness with the increase in flexible pad hardness is an intriguing behavior. During plastic deformation in FPLSF, the shockload acts on the top surface of the
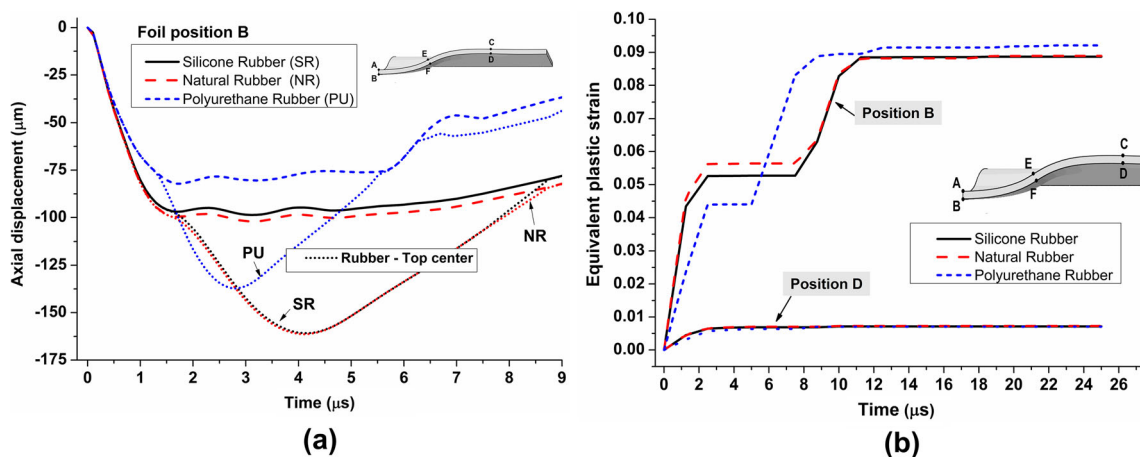
Fig. 10 Comparison of **a** axial displacement (μm) of foil position B and rubber top center, **b** equivalent plastic strain between foil positions B and D, between different flexible pad materials
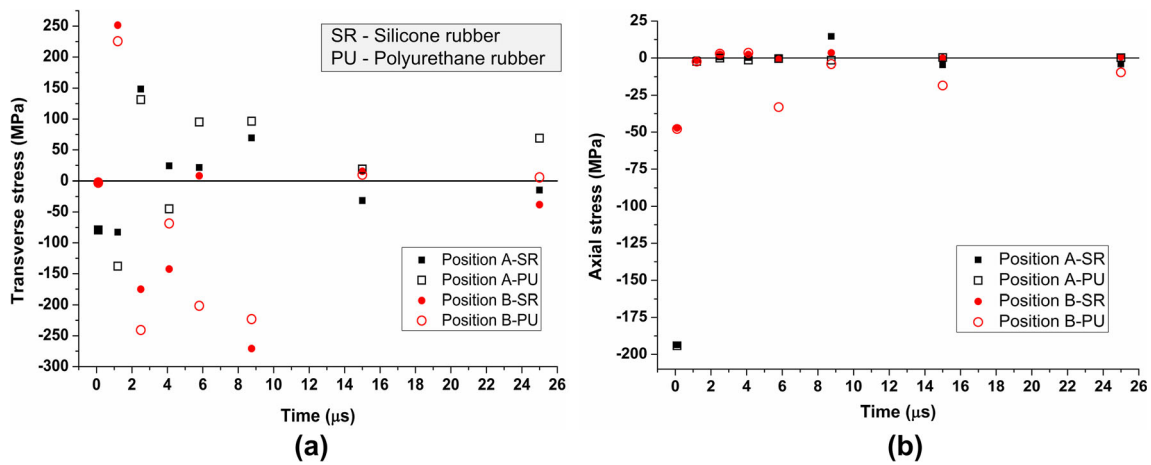
Fig. 11 Effect of flexible pad hardness on stress distribution at foil positions A (top surface) and B (bottom surface) **a** transverse stress, **b** axial stress [SR – Silicone Rubber; PU – Polyurethane Rubber]

metal foil during its entire duration. Meanwhile, the bottom surface of the foil will be experiencing resistance against the deformation from the flexible pad. With increase in flexible pad hardness, there will be more resistance to the foil deformation causing compression of the foil in the thickness direction. Thus, the foil is expected to experience more compression, and hence an increase in foil thinning and surface hardness when the pad hardness is increased. The observed experimental results with opposite trends can be examined by stress-strain distribution at the top and bottom foil surfaces.

Figure 11 compares the schematic of stress profiles between silicone rubber and polyurethane rubber at the center of crater top and bottom surfaces for copper foils during FPLSF. Before the foil deformation is started (at 100 ns), both axial and transverse stresses at the foil positions A and B are compressive and remain identical, for both pad materials. With increase in flexible pad hardness, both foil positions A and B experience more compression along axial and transverse directions during deformation at 1.25 μs. The axial stress remains compressive throughout whereas transverse stress shifts between tension and compression during deformation. For all processing

conditions, the magnitude of axial stress is much smaller than that of transverse stresses, as evident from Fig. 11.

The above-mentioned stress-strain distribution can be used to explain the observed experimental behavior of thinning. Thinning of metal foils usually occurs due to a combined compressive axial strain and tensile transverse strains. As the axial strain remains compressive and transverse strains remain tensile throughout the deformation during FPLSF (Fig. 12), metal foils experience thinning. As the magnitude of the axial and transverse strains at the center is larger than that of strains at other foil positions, maximum thinning occurs at the center of the crater. The reduction in thinning with increase in flexible pad hardness is attributed to the following behaviors:

- During FPLSF, as the magnitudes of both the axial compressive strain and transverse tensile strain decrease with increase in flexible pad hardness, a reduction in thinning is expected.
- It is noticed from Fig. 10 that, though the final crater depth is controlled by the flexible pad, axial displacement of the flexible pad continues even after the foil deformation
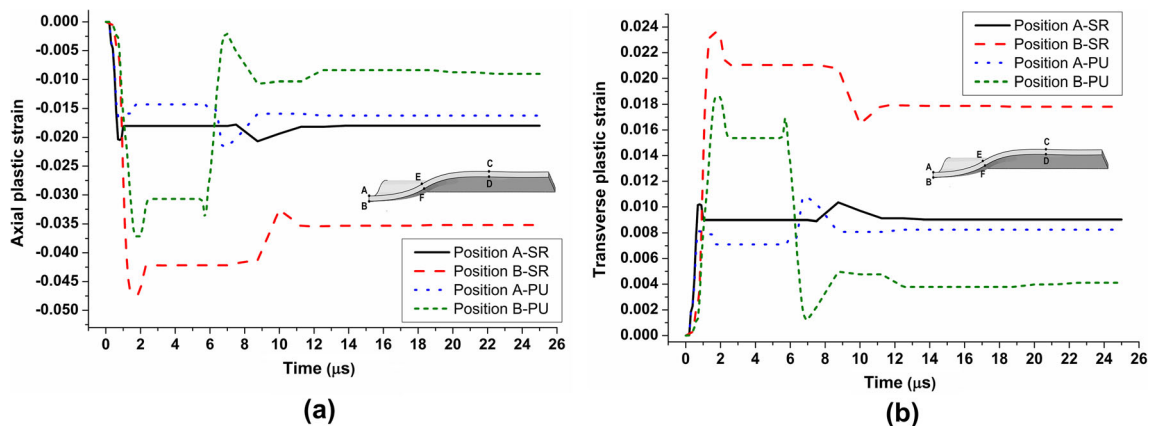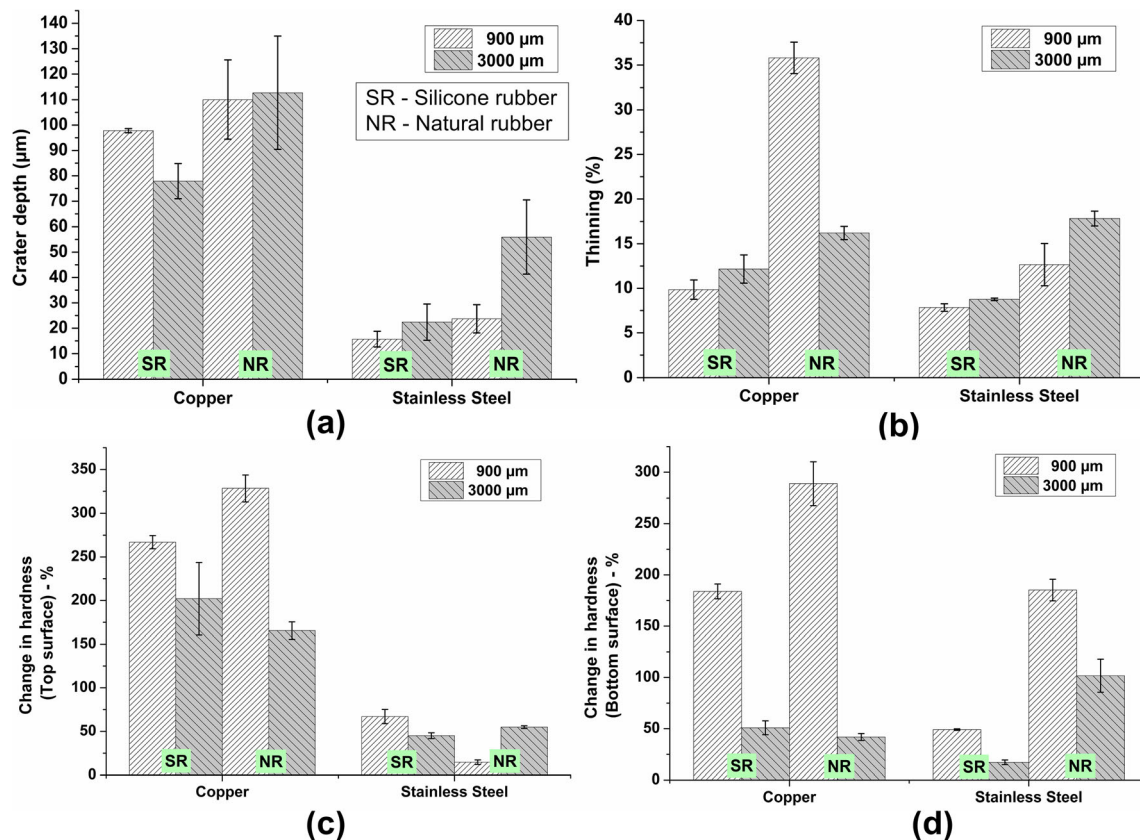

Fig. 12 Effect of flexible pad hardness on strain distribution at the foil positions A and B **a** transverse plastic strain, **b** axial plastic strain [SR – Silicone Rubber; PU – Polyurethane Rubber]

ceases, irrespective of the pad material. Due to the departure of the flexible pad from the bottom surface, there will be no axial compression of foil as expected.

Similarly, the observation of reduced surface hardness with increase in the flexible pad hardness is attributed to the following factors: (a) the residual stresses at the center of both the top and bottom surfaces change from compressive (with silicone rubber) to tensile (with polyurethane rubber) with increase in pad hardness (Fig. 11). Due to the absence of compressive residual stresses, hardness could be reduced with polyurethane rubber, (b) reduction in axial compressive strain and transverse tensile strains are observed (Fig. 12) with increase in pad hardness together with lesser plastic deformation, which could have resulted in the reduction of surface hardness.
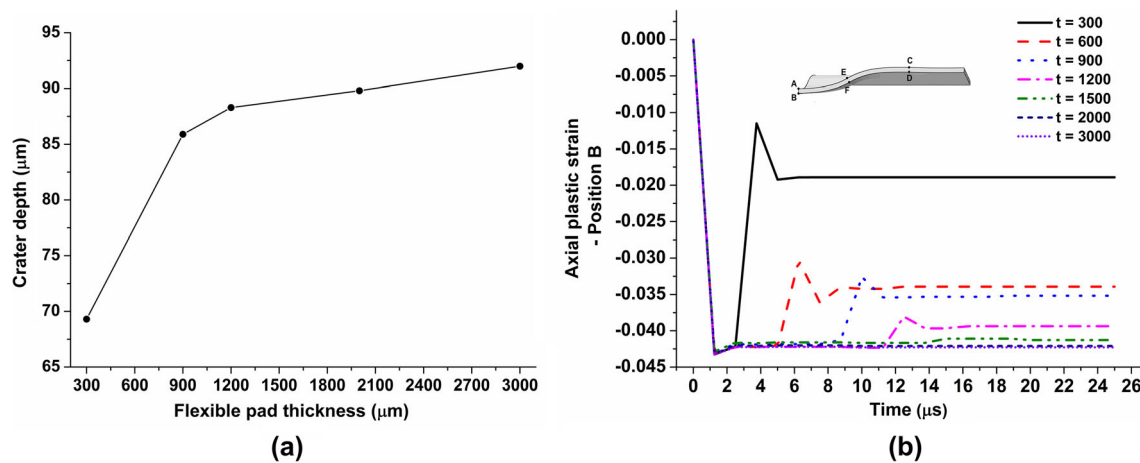
Effect of flexible pad thickness

Figure 13 compares the experimental results of crater depth, foil thinning at crater center, and the top and bottom crater surface hardness between two flexible pad thicknesses, 900 μm and 3000 μm, for different foil materials and flexible pads.

For increase in the pad thickness from 900 μm to 3000 μm, the crater depth increased from 110 μm to 112.7 μm for copper foil, whereas a large increase from 23.7 μm to 55.9 μm occurred for stainless steel foils with natural rubber pad. This behavior of pad thickness is identical with silicone rubber, despite a discrepancy in copper foil. Thus, it can be identified that the crater depth increased along with the increase in pad thickness.

The finite element analysis of the effect of flexible pad thickness on the foil deformation is performed at following thickness levels: 300 μm, 600 μm, 900 μm, 1200 μm, 1500 μm, 2000 μm, and 3000 μm. Silicone rubber is used as the flexible pad. The change in crater depth with the change in pad thickness is plotted in Fig. 14a. For increase in the pad thickness, the crater depth increases drastically from 300 μm to 900 μm, whereas it becomes gradual for thicknesses greater than 900 μm. Though the crater depth increases significantly along with the pad thickness, it is interesting to observe that the maximum displacement at the foil positions A and B at 1.25 μs remains unchanged, which can be witnessed from identical axial plastic strain in Fig. 14b. The constant axial displacement with the change in pad thickness can be attributed to the dependence of the foil displacement on the laser-induced shock pressure and the flexible pad properties, which are kept constant in this analysis.

Fig. 13 Experimental investigation of the effect of flexible pad thickness on a crater depth, b foil thinning at crater center, c crater top surface hardness at center, d crater bottom surface hardness at center [SR – Silicone Rubber; PU – Polyurethane Rubber]

Fig. 14 Finite element analysis of the flexible pad thickness influence in FPLSF **a** change in crater depth with respect to the flexible pad thickness, **b** evolution of axial plastic strain at foil position B with change in pad thickness

A significant difference in elastic recovery of the flexible pad is found to occur with the change in pad thickness. During the foil deformation stage, disengagement of the flexible pad from the metal foil is accompanied by the propagation of an axial compressive shockwave starting from the flexible pad top surface through its thickness. Subsequently, a tensile wave is formed at the flexible pad top surface at 5 μs as shown in Fig. 15a. As a result, contact between the pad and the foil is established at foil position B, causing an upward displacement of the contact region. During this stage, compressive wave in the axial direction is reflected back from the pad bottom, forcing the pad to detach from the metal backing. Concurrent propagation of the transverse tensile shockwave causes the flexible pad to establish contact with the foil initially at the crater center and then at the circumference (position F) and the non-deformed area (position D). Fig. 15b shows the contact formation between the flexible pad and the foil with 900 μm pad thickness. The above-mentioned phenomenon is found to occur for the pad thickness ranging between 900 μm and 1500 μm. If the flexible pad is thicker than 1500 μm, the contact is established only between foil positions B and F, as shown in Fig. 15b for 3000 μm, as the compressive shockwave takes longer time to reach the bottom surface. Correspondingly, no compression of the foil position B can be noticed from Fig. 14b for pad thicknesses greater than 1500 μm. Therefore, it is evident that the interaction between different shockwaves, axial rarefaction wave and transverse tensile waves, during the flexible pad elastic recovery has a decisive role in the final crater geometry. As the flexible pad thickness influences the axial rarefaction wave, it is a significant factor for crater depth, crater shape, foil thinning, and the crater surface hardness in FPLSF.

The change in elastic recovery of flexible pad with thickness can be attributed to the observed change in crater depth (Fig. 14a). The smaller crater depth with 300 μm could be

attributed to larger plastic deformation in the opposite direction due to the early elastic recovery and the flexible pad detachment, which can be verified from the corresponding larger axial plastic strain shown in Fig. 14b. The reduction of surface hardness with an increase in flexible pad hardness can be explained based on the following behaviors: (a) It can be noticed from Fig. 14b that the amount of plastic deformation at the foil center during elastic recovery of the pad reduces with the increase in pad thickness, and almost no deformation is observed for pad thicknesses greater than 2000 μm, (b) with increase in pad thickness, the magnitude of compressive residual stresses remains approximately constant at the center of the top surface (Fig. 16a), whereas the residual stresses change from compressive to tensile at the center of the bottom surface (Fig. 16b). As both the magnitudes of plastic deformation and compressive residual stresses reduce with the increase in pad thickness, the surface hardness experienced a reduction. Therefore, while comparing the effect of pad thickness of crater depth with that of surface hardness, it is realized that, an optimum thickness of flexible pad has to be selected in order to achieve maximum feature deformation and maximum surface hardness of formed features.
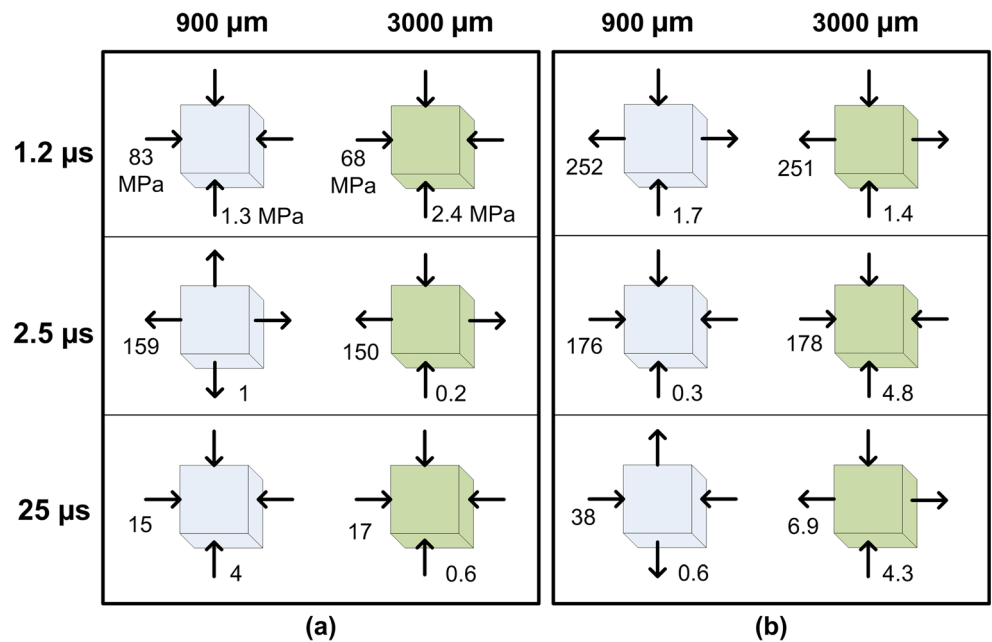
Conclusions

This paper reports on the experimental and finite element analysis of the influence of flexible pad hardness and its thickness on the plastic deformation of thin metal foils in Flexible Pad Laser Shock Forming (FPLSF). The developed FE model predicts the depth, diameter and shape of the craters reasonably well with that of experiments. Crater formation in FPLSF is classified into four different stages. The experimental and FE analysis highlighted a significant influence of the hardness

Fig. 15 **a** Axial strain contour indicating different shockwaves at 5 μs (thickness - 900 μm), **b** comparison of contact evolution between the foil and the flexible pad during elastic recovery, for pad thicknesses 900 μm and 3000 μm

(a)

(b)
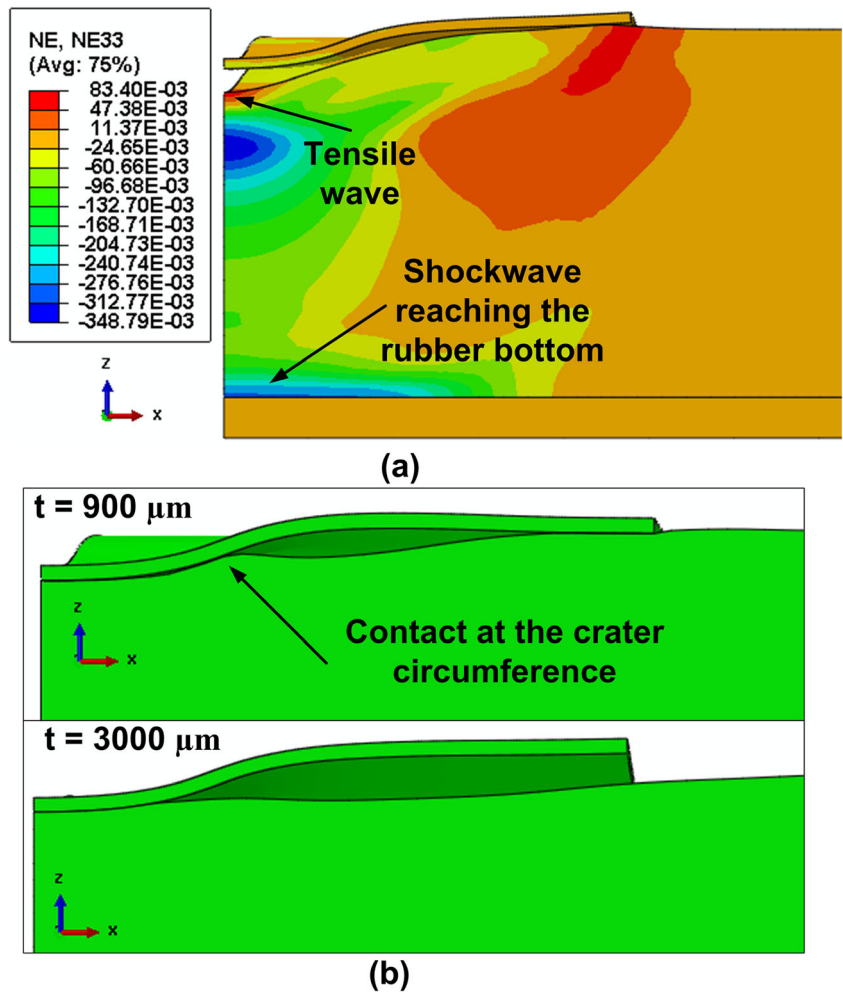
Fig. 16 Effect of flexible pad thickness on stress distributions (unit as MPa) of the metal foil during deformation at **a** position A (top surface), **b** position B (bottom surface)

and thickness of the flexible pad. The following conclusions can be derived from the results:

- The increase in flexible pad hardness resulted in the reduction of crater depth, foil thinning and the hardness at the top and bottom crater surfaces.
- The increase in flexible pad thickness caused an increase in crater depth and thinning but a reduction in surface hardness. An optimum pad thickness exists to maximize the feature deformation with enhanced surface hardness.
- The flexible pad thickness affects the elastic recovery of the flexible pad, which hence influences the change in crater depth, due to the relative displacement of different foil positions.
- The difference in the geometry and surface characteristics of the deformation features with change in flexible pad hardness and thickness is attributed to the magnitude and direction of strain distribution during the deformation stage, additional plastic deformation during elastic recovery of the flexible pad, and residual stress distributions at the deformed feature.

Future studies will focus on the detailed microstructural analysis, interaction of various process parameters, and the finite element modelling improvement for the better prediction of FPLSF process.

References

1. Nagarajan B, Castagne S, Wang Z (2013) Mold-free fabrication of 3D microfeatures using laser-induced shock pressure. Appl Surf Sci 268 (0):529–534. doi:10.1016/j.apsusc.2012.12.163

2. Nagarajan B, Castagne S, Wang Z (2013) Influence of Process Parameters on the Deformation of Copper Foils in Flexible-Pad Laser Shock Forming. Paper presented at the 8th International Conference on MicroManufacturing, University of Victoria, Victoria BC, Canada

3. Ramezani M, Ripin ZM, Ahmad R (2010) Sheet metal forming with the aid of flexible punch, numerical approach and experimental validation. CIRP J Manuf Sci Technol 3(3):196–203. doi:10.1016/j.cirpj.2010.11.002

4. Liu Y, Hua L, Lan J, Wei X (2010) Studies of the deformation styles of the rubber-pad forming process used for manufacturing metallic bipolar plates. J Power Sources 195(24):8177–8184. doi:10.1016/j.jpowsour.2010.06.078

5. Thiruvarudchelvan S (1993) Elastomers in metal forming: a review. J Mater Process Technol 39(1–2):55–82. doi:10.1016/0924-0136(93)90008-t

6. Liu Y, Hua L (2010) Fabrication of metallic bipolar plate for proton exchange membrane fuel cells by rubber pad forming. J Power Sources 195(11):3529–3535. doi:10.1016/j.jpowsour.2009.12.046

7. Peng L, Hu P, Lai X, Mei D, Ni J (2009) Investigation of micro/meso sheet soft punch stamping process – simulation and experiments. Mater Des 30(3):783–790. doi:10.1016/j.matdes.2008.05.074

8. Peng L, Ni J, Liu Da HP, Lai X (2010) Fabrication of metallic bipolar plates for proton exchange membrane fuel cell by flexible forming process-numerical simulations and experiments. J Fuel Cell Sci Tech 7(3):031009–031009. doi:10.1115/1.3207870

9. Dirikolu MH, Akdemir E (2004) Computer aided modelling of flexible forming process. J Mater Process Technol 148(3):376–381. doi:10.1016/j.jmatprotec.2004.02.049

10. Wang X, Du D, Zhang H, Shen Z, Liu H, Zhou J, Liu H, Hu Y, Gu C (2013) Investigation of microscale laser dynamic flexible forming process - simulation and experiments. Int J Mach Tools Manuf 67(0):8–17. doi:10.1016/j.ijmachtools.2012.12.003

11. Lim SS, Kim YT, Kang CG (2013) Fabrication of aluminum 1050 micro-channel proton exchange membrane fuel cell bipolar plate using rubber-pad-forming process. Int J Adv Manuf Technol 65(1–4):231–238. doi:10.1007/s00170-012-4162-8

12. Watari H, Ona H, Yoshida Y (2003) Flexible punching method using an elastic tool instead of a metal punch. J Mater Process Technol 137(1–3):151–155. doi:10.1016/s0924-0136(02)01080-4

13. Son C-Y, Jeon Y-P, Kim Y-T, Kang C-G (2012) Evaluation of the formability of a bipolar plate manufactured from aluminum alloy Al 1050 using the rubber pad forming process. Proc Inst Mech Eng Part B-J Eng Manuf. doi:10.1177/0954405411434446

14. Sala G (2001) A numerical and experimental approach to optimise sheet stamping technologies: part II – aluminium alloys rubber-forming. Mater Des 22(4):299–315. doi:10.1016/s0261-3069(00)00088-1

15. Ramezani M, Ripin ZM (2012) Analysis of deep drawing of sheet metal using the marform process. Int J Adv Manuf Technol 59(5):491–505. doi:10.1007/s00170-011-3513-1

16. Fabbro R, Fournier J, Ballard P, Devaux D, Virmont J (1990) Physical study of laser-produced plasma in confined geometry. J Appl Phys 68(2):775–784. doi:10.1063/1.346783

17. Zhang W, Yao YL (2002) Micro scale laser shock processing of metallic components. J Manuf Sci Eng -Trans ASME 124(2):369–378. doi:10.1115/1.1445149

18. Liu H, Shen Z, Wang X, Wang H (2009) Numerical simulation and experimentation of a novel laser indirect shock forming. J Appl Phys 106(6):063107. doi:10.1063/1.3212992

19. Devaux D, Fabbro R, Tollier L, Bartnicki E (1993) Generation of shock waves by laser-induced plasma in confined geometry. J Appl Phys 74(4):2268–2273. doi:10.1063/1.354710

20. Johnson GR, Cook WH (1983) A constitutive model and data for metals subjected to large strains, high strain rates, and high temperatures. Proceedings of Seventh International Symposium on Ballistics, The Hague, The Netherlands, pp. 541–547

21. Bae G, Xiong Y, Kumar S, Kang K, Lee C (2008) General aspects of interface bonding in kinetic sprayed coatings. Acta Mater 56(17):4858–4868. doi:10.1016/j.actamat.2008.06.003

22. Tounsi N, Vincenti J, Otho A, Elbestawi MA (2002) From the basic mechanics of orthogonal metal cutting toward the identification of the constitutive equation. Int J Mach Tools Manuf 42(12):1373–1383. doi:10.1016/S0890-6955(02)00046-9

23. Martins PALS, Natal Jorge RM, Ferreira AJM (2006) A comparative study of several material models for prediction of hyperelastic properties: application to silicone-rubber and soft tissues. Strain 42(3):135–147. doi:10.1111/j.1475-1305.2006.00257.x

24. Fabbro R, Peyre P, Berthe L, Scherpereel X (1998) Physics and applications of laser-shock processing. J Laser Appl 10(6):265–279. doi:10.2351/1.521861

25. Nagarajan B, Wang Z, Castagne S, Zheng H (2014) Investigation of laser-induced plasma evolution in flexible pad laser shock forming with high speed camera. Appl Surf Sci 308:221–229. doi:10.1016/j.apsusc.2014.04.139